RSC Advances

PAPER

View Article Online
View Journal | View Issue

Cite this: *RSC Adv.*, 2026, **16**, 3138

Distribution of polychlorinated organic by-products during the hydrolytic oxidation of chlorinated volatile organic pollutants over Pd–Ni-based catalysts

Yuqing Li, Bisi Lv, Na Li,* Wenjie Song, Jiahui Zhou, Caifei Ni, Wenlong Fu and Zhen Han

Hydrolytic oxidation has been proven to effectively minimize the formation of polychlorinated organic by-products during the catalytic degradation of chlorinated volatile organic pollutants (CVOCs). In this study, we delved into the distribution characteristics of chlorinated organic by-products that occur during the hydrolytic oxidation of chlorobenzene, 1,2-dichlorobenzene, and *o*-chlorophenol. When it came to the catalytic degradation of chlorobenzene and 1,2-dichlorobenzene, we detected a small quantity of chlorinated organic by-products. Notably, both the types and concentrations of these by-products exhibited a volcano-type trend with increasing temperature, which was attributed to the competition between CVOC degradation and by-product formation at different temperature stages. On the other hand, during the catalytic degradation of *o*-chlorophenol, no aromatic chlorinated organic by-products were found at all. The 0.5% Pd–10% Ni/ZSM-5(25) catalyst stood out with the best hydrolytic oxidation activity. Specifically, the complete conversion temperatures for *o*-chlorophenol, chlorobenzene, and 1,2-dichlorobenzene were 250 °C, 375 °C, and 425 °C respectively. We employed various analytical techniques such as XRD, XPS, FTIR, H_2O-TPD, and pyridine-FTIR to explore the impact of the structure and surface properties of modified ZSM-5 zeolites on catalytic activity. The study revealed that the catalytic activity mainly stems from the surface acidity, active protons and the redox properties of the catalyst.

Received 3rd November 2025
Accepted 6th January 2026

DOI: 10.1039/d5ra08447d

rsc.li/rsc-advances

1 Introduction

Chlorinated volatile organic pollutants (CVOCs) are one of the important pollutants in the atmosphere, and they participate in photochemical reactions to form harmful substances such as ozone and secondary organic aerosols, which contribute to atmospheric pollution.[1,2] Ozone has adverse effects on human health and plant growth, while secondary organic aerosols affect atmospheric visibility and contribute to climate change. CVOCs can enter soil and water bodies through atmospheric deposition and wastewater discharge. In the soil, they may affect soil fertility and microbial communities and adversely affect crop growth. When entering water bodies, they can be toxic to aquatic organisms and disrupt the balance of aquatic ecosystems.[3,4]

Due to the wide concentration range and large volume of CVOC industrial exhaust emissions, catalytic oxidation is the most thorough and effective treatment technology for CVOC treatment among the current mainstream volatile organic compound (VOC) control technologies in terms of the economic cost of treatment and the feasibility of efficient and safe industrialization.[5–7] Researchers have studied this extensively, with most studies focusing on advanced catalyst design and understanding the intrinsically active reaction centers.[8,9] However, the C–Cl bond in CVOCs replaces the C–H bond in VOCs, and from the thermodynamic point of view, the C–Cl bond is easier to break, which makes it easier to catalyze the oxidation of CVOCs.[10] But in reality, it is not the case, and the Cl species generated in the process of catalytic oxidation of CVOCs can easily be enriched on the surface of the catalyst to cause chlorine toxicity of the catalyst, which leads to the deactivation of the catalyst;[11,12] moreover, the Cl species on the surface of the catalyst reacts with the hydrocarbons to generate more toxic by-products, resulting in secondary pollution.[13,14]

It was found that polychlorinated organic pollutants ($PhCl_x$) was not only generated during the catalytic oxidation of loaded noble metal catalysts, but was still detected during the catalytic oxidation of CVOCs with transition metal complex oxides. Gu *et al.*[15] investigated the decomposition of chlorobenzene (CB) over WO_x/CeO_2 catalysts and detected 1,2,4-trichlorobenzene

College of Safety and Environmental Engineering, Shandong University of Science and Technology, Qingdao, Shandong Province, 266590, P. R. China. E-mail: lina@sdust.edu.cn

(1,2,4-$PhCl_3$) and 1,3,5-trichlorobenzene (1,3,5-$PhCl_3$). Weng *et al.*[16,17] detected chlorinated hydrocarbons and chlorinated aromatic hydrocarbons in the tail gas of catalytic oxidation of CB using $Mn_xCe_{1-x}O_2$/H-ZSM5 as catalyst. Deng *et al.*[18] were able to detect dichlorobenzene in the catalytic oxidation of CB with cobalt-based composite oxides Co/M = 3 (M = Al, Fe, Cr), and the selectivity of the reactant tail gas, Cl_2, was able to reach 30%. Besides, Wang *et al.*[19] currently generated CB during the catalytic oxidation process of *o*-dichlorobenzene.

The current stage of research indicates that the formation of polychlorinated organic compounds is mainly related to the formation of metal M–O–Cl bonds by Cl species on the catalyst surface.[20–23] The metal M–O–Cl species undergo electrophilic substitution chlorination reactions with reactants adsorbed on the catalyst surface, followed by desorption to form polychlorinated organic pollutants. Our previous studies hypothesized that oxygen molecules are chemisorbed on the surface of the Pd(I)Cl species and undergo electron transfer from the Pd(I)Cl species to O_2 *via* an electrophilic substitution reaction to form reactive oxygen species.[24] The reactive oxygen species then undergoes an oxidation reaction with the chlorine atom attached to the palladium to form hypochlorite. At the same time, positively charged chlorine atoms can react with adsorbed chlorophenolic species *via* electrophilic substitution to form polychlorinated organic compounds.

Therefore, based on the above findings, the rapid removal of Cl species from the catalyst surface is a critical factor in solving the catalyst poisoning and the generation of polychlorinated organic compounds. Our previous research found that adding water to the reaction atmosphere can effectively reduce the generation of polychlorinated organic by-products.[25] Recently, it was also found that the positive roles of water vapor may contribute to achieve no or low polychlorinated by-product selectivity is essential for the CVOCs degradation.[26] Therefore, we have reason to believe the hydrolytic oxidation reaction can not only completely catalytic degradation of chlorinated organic pollutants, but also effectively inhibit the formation of chlorine-containing organic by-products.[27,28]

Recent research has demonstrated that Ni exhibits excellent catalytic performance in hydrolysis reaction.[29–31] Ni not only adsorbs and activates H_2O but also facilitates the activation and decomposition of organic compounds. It has been reported that the strong interaction between Ni and other metals promotes the formation of H_2O-active sites,[32] which plays a dominant role in determining the catalyst's activity. A synergistic effect exists between Pd and Ni. This synergy further enhances the catalyst's activity, selectivity, and stability. By adjusting parameters such as the Pd–Ni loading amounts, the performance of Pd–Ni bimetallic catalysts can be finely tuned to meet the demands of the hydrolytic oxidation reactions of CVOCs. H-type molecular sieve catalysts are considered as potential materials for the catalytic oxidation of CVOCs, and their catalytic oxidation performance towards chlorinated aromatic compounds was investigated. Therefore, in this study, ZSM-5(25) (the SiO_2/Al_2O_3 ratio is 25) was selected as the catalyst support.

In this study, 0.5% Pd/ZSM-5(25), 10% Ni/ZSM-5(25) and 0.5% Pd–10% Ni/ZSM-5(25) were used as model catalysts, and 1,2-dichlorobenzene (1,2-DCB), CB, and *o*-chlorophenol were continued to be selected as model pollutants. The distribution of species and concentrations of organic and inorganic products generated at different reaction temperatures was detected. The physicochemical properties of the materials were analyzed by XPS (X-ray Photoelectron Spectrometer), XRD (X-ray Diffraction), FTIR (Fourier Transform Infrared spectroscopy), H_2O-TPD (Programmed Thermal Desorption) and pyridine-FTIR (Pyridine-Fourier Transform Infrared spectroscopy) experiments. The influence of physicochemical properties of Pd–Ni-based catalysts on hydrolytic oxidation activity was investigated. The primary contribution of this work lies in the systematic elucidation of the distribution characteristics of chlorinated organic by-products during catalytic degradation of CVOCs, as well as the in-depth analysis of the structure–activity relationships between the bimetallic Pd–Ni active sites, the ZSM-5 support properties, and the catalytic performance. These findings provide fundamental insights for the rational design of high-efficiency and low-by-product catalysts for CVOCs catalytic degradation.

2 Experiments

2.1 Catalyst preparation

The loaded Pd–Ni based catalysts were prepared by equal volume impregnation method. For Pd, a series of tests with loadings ranging from 0.1 to 0.5 wt% showed that CVOC degradation efficiency increased with rising Pd content; considering the cost constraints of this noble metal, 0.5 wt% was determined as the optimal Pd loading. For Ni, catalytic performance was evaluated across the 5–15 wt% range, and 10 wt% was identified as the ideal loading to strike a balance between catalytic activity and raw material cost. The loadings of the Pd and Ni were 0.5% Pd, 10% Ni and 0.5% Pd–10% Ni. The $Pd(NO_3)_2$ and $Ni(NO_3)_2 \cdot 6H_2O$ were pipetted from the loading calculations and diluted to the corresponding impregnation volume of the carriers with ultrapure water, and then the ZSM-5(25) (the SiO_2/Al_2O_3 ratio is 25) carriers were added into a beaker, and the mixture was mixed well by stirring for 10 min and ultrasound for 15 min to make the mixture homogeneous. The impregnated solid was dried at 80 °C for 12 h. After drying, the samples were roasted in air at 600 °C (with a heating rate of 5 °C min^{-1}) for 4 h. The roasted samples were reduced in H_2 atmosphere at 450 °C for 2 h (with a heating rate of 3 °C min^{-1}).

2.2 Catalyst characterization

The crystal structure was detected by XRD. XRD spectra were conducted on an X'pert PRO equipment using Cu Kα radiation (λ = 0.15418 nm). The data was collected in a 2θ range of 5–90°.

The elemental composition and chemical valence states of the sample surfaces were tested on a Thermo ESCALAB 250 XPS using Al Kα as the excitation source for X-rays and the C 1s binding energy peak as the internal standard (binding energy of 284.6 eV) and the test error was in ±0.2 eV.

The FTIR spectrum of the sample was obtained by testing on a Nicolet 8700 Fourier Transform Infrared spectrometer. The

scanning range is 500–4500 cm^{-1}, with a scanning step size of 2.14 cm^{-1}. Before testing, take a small amount of sample mixed with KBr and press it into a semitransparent thin sheet.

The pyridine-FTIR spectroscopic studies were carried out on a Nicolet 6700 IR spectrometer equipped with a photoconductive (MCT) detector. First, the samples were treated *in situ* under vacuum at 500 °C for 1 h and then cooled to room temperature. Pyridine vapor was introduced into the transmission cell and the physically adsorbed pyridine was withdrawn. Finally, the samples were heated to 150 °C, 250 °C, 350 °C and 450 °C and the spectra were recorded.

H_2O-TPD experiments were carried out on chemisorption model 2920. Before each experiment, 100 mg of the sample was pretreated in He gas at 50 mL min^{-1} for 1 h at 300 °C. After cooling to 50 °C, 3.2 vol% H_2O/He was introduced until adsorption was saturated, and then the sample was heated from 50 °C to 700 °C in He gas at a ramping rate of 10 °C min^{-1} at 50 mL min^{-1}.

2.3 Catalytic performance evaluation

The catalytic performance of the catalyst for 1,2-DCB was evaluated using a fixed-bed continuous flow VOC catalytic oxidation reaction unit, and the composition of the feedstock and products was obtained by gas chromatography and on-line analysis by upper FTIR spectrometer (as specified in the SI). The reaction gas composition was 500 ppm 1,2-DCB (500 ppm CB or 500 ppm *o*-chlorophenol), 3.2 vol% H_2O (according to the results of our previous work[25]) and balance N_2. The total gas flow rate is 250 mL min^{-1}, the gas space velocity (GHSV) is 15 000 h^{-1}, and the temperature range is 200 to 500 °C (100 to 450 °C or 50 to 300 °C).

Regarding the calculation of each set of data, we take the calculation of 1,2-dichlorobenzene as an example, and the details are as follows.

The conversion of 1,2-DCB catalytic oxidation is calculated as eqn (1),

$$X_{1,2\text{-DCB}} = \frac{[1,2\text{-DCB}]_{in}\ \text{vol\%} - [1,2\text{-DCB}]_{out}\ \text{vol\%}}{[1,2\text{-DCB}]_{in}\ \text{vol\%}} \quad (1)$$

where $[1,2\text{-DCB}]_{in}$ and $[1,2\text{-DCB}]_{out}$ are the 1,2-DCB concentrations in the inlet and outlet gas (vol%), respectively.

The yields of CO, CO_2 and CO_x is calculated as eqn (2), (3) and (4), respectively.

$$Y_{CO} = \frac{[CO]_{out}\ \text{vol\%}}{6[1,2\text{-DCB}]_{in}\ \text{vol\%}} \quad (2)$$

$$Y_{CO_2} = \frac{[CO_2]_{out}\ \text{vol\%}}{6[1,2\text{-DCB}]_{in}\ \text{vol\%}} \quad (3)$$

$$Y_{CO_x} = \frac{[CO]_{out}\ \text{vol\%} + [CO_2]_{out}\ \text{vol\%}}{6[1,2\text{-DCB}]_{in}\ \text{vol\%}} \quad (4)$$

where $[CO]_{out}$ and $[CO_2]_{out}$ are the CO and CO_2 concentrations in outlet gas (vol%).

The reaction rate ($r_{1,2\text{-DCB}}$, mol s^{-1} g^{-1}) was calculated as eqn (5),

$$r_{1,2\text{-DCB}} = \frac{c_{1,2\text{-DCB}} X_{1,2\text{-DCB}} V p_{atm}}{m_{cat.} RT}\ \left(\text{mol s}^{-1}\ \text{g}^{-1}\right) \quad (5)$$

where $m_{cat.}$ = catalyst weight, $c_{1,2\text{-DCB}}$ = concentration of 1,2-DCB, V = total flow rate, $X_{1,2\text{-DCB}}$ = 1,2-DCB conversion, R = 8.314 Pa m^3 mol^{-1} K^{-1}, T = room temperature, p_{atm} = 101.3 kPa.

The empirical kinetic expression of the reaction rate can be calculated as eqn (6),

$$r_{1,2\text{-DCB}} = A \exp\left(-\frac{E_a}{RT}\right) p_{1,2\text{-DCB}}{}^{\alpha} p_{O_2}{}^{\beta} \quad (6)$$

The eqn (7) can be gained by logarithmic transformation.

$$\ln r_{1,2\text{-DCB}} = \ln A + \alpha \ln p_{1,2\text{-DCB}} + \beta \ln p_{O_2} - E_a/(RT) \quad (7)$$

In the process of the kinetics research, the concentration of 1,2-DCB and O_2 almost never changes when the conversion of 1,2-DCB is <15%, hence, $\ln A$, $\alpha \ln p_{1,2\text{-DCB}}$ and $\beta \ln p_{O_2}$ can be approximated as constants, eqn (8) can be obtained.

$$\ln r_{1,2\text{-DCB}} = -\frac{E_a}{RT} + C \quad (8)$$

The activation energy (E_a) can be achieved from the slope of the resulting linear plot of $\ln r$ *versus* $1/T$.

The "chlorine equilibrium rate" is defined as the ratio of the total amount of chlorine detected in all measured products (including HCl, Cl_2, and chlorinated organic by-products) to the initial amount of chlorine in the fed CVOCs. A value of 100% indicates a complete chlorine balance, meaning all chlorine in the reactants has been accounted for in the detected products.

3 Results and discussion

3.1 1,2-DCB catalytic degradation activity and product distribution

The catalytic performance of 0.5% Pd/ZSM-5(25), 10% Ni/ZSM-5(25), and 0.5% Pd–10% Ni/ZSM-5(25) was evaluated for the hydrolytic oxidation of 500 ppm 1,2-dichlorobenzene (1,2-DCB) under a reaction atmosphere containing 3.2 vol% H_2O, with the conversion profiles depicted in Fig. 1. For all the investigated catalysts, 1,2-DCB conversion was found to increase monotonically with elevating reaction temperature within the experimental temperature window. Specifically, the 0.5% Pd–10% Ni/ZSM-5(25) catalyst achieved complete 1,2-DCB conversion (100%) at 450 °C, whereas 10% Ni/ZSM-5(25) reached full conversion at an elevated temperature of 475 °C. In sharp contrast, even at the highest tested temperature of 500 °C, the 0.5% Pd/ZSM-5(25) catalyst only reached a maximum conversion efficiency of 97%. The temperatures corresponding to 90% conversion ($T_{90\%}$) for 0.5% Pd/ZSM-5(25), 10% Ni/ZSM-5(25), and 0.5% Pd–10% Ni/ZSM-5(25) were determined to be 469, 397, and 394 °C, respectively.

Notably, the bimetallic 0.5% Pd–10% Ni/ZSM-5(25) catalyst delivered the highest reaction rate of 2.44 mmol g^{-1} s^{-1} at 250 °C, accompanied by the lowest activation energy of 44.3 kJ mol^{-1},

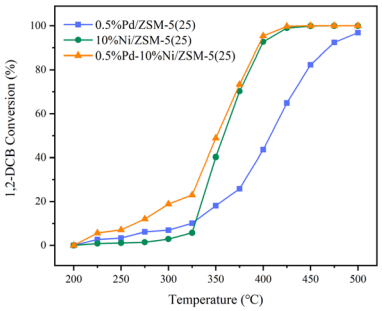

Fig. 1 1,2-DCB hydrolytic oxidation activity curve.

thus highlighting its superior low-temperature catalytic activity, reaction efficiency, and kinetic accessibility. The monometallic 0.5% Pd/ZSM-5(25) catalyst displayed moderate catalytic performance in terms of the aforementioned parameters. In sharp contrast, 10% Ni/ZSM-5(25) exhibited the highest full-conversion temperature, maximum activation energy, and minimal reaction rate, indicative of the weakest overall catalytic activity among the three catalysts. It is worth noting that when the reaction temperature exceeded 325 °C, the catalytic activity of the investigated catalysts followed the descending order: 0.5% Pd–10% Ni/ZSM-5(25) > 10% Ni/ZSM-5(25) > 0.5% Pd/ZSM-5(25).

The main inorganic products from the catalytic degradation of 1,2-DCB were CO, CO_2, HCl and H_2O. Their distribution over 0.5% Pd/ZSM-5(25), 10% Ni/ZSM-5(25) and 0.5% Pd–10% Ni/ZSM-5(25) catalysts at different temperatures is shown in Fig. 2 and S1. Throughout the tested temperature range, CO_2 yield was far lower than that of CO and only formed at higher temperatures. For all catalysts, CO yield remained low below 325 °C, then rose rapidly with increasing temperature. CO_2 yield increased slowly up to 375 °C, after which its growth slowed further. Below 325 °C, 0.5% Pd–10% Ni/ZSM-5(25) exhibited lower CO yield than the other two catalysts. However, at 350 °C and above, its CO yield surpassed that of the monometallic catalysts and continued to rise with temperature.

At the reaction temperature of 500 °C, the three catalysts exhibit a significant difference in CO_x selectivity: the CO_x selectivity of catalyst 0.5% Pd–10% Ni/ZSM-5(25) reaches as high as 100%, demonstrating its excellent performance in the complete mineralization of 1,2-DCB into CO_x. In contrast, the CO_x selectivity of 10% Ni/ZSM-5(25) and 0.5% Pd/ZSM-5(25) catalyst is only 94% and 89%, respectively, indicating that partial carbon sources are converted into organic by-products during their catalytic degradation process, and the complete degradation of the target pollutant is not achieved.

In the reaction temperature range, the selectivity of each catalyst for HCl increased continuously with increasing temperature, among which the 0.5% Pd–10% Ni/ZSM-5(25) catalyst showed strong selectivity for HCl generation. When the temperature reached 475 °C, the HCl generation by 10% Ni/ZSM-5(25) and 0.5% Pd–10% Ni/ZSM-5(25) catalysts was slightly decreased, while for 0.5% Pd/ZSM-5(25), the HCl generation was continuously increased, which was consistent with the hydrolytic oxidation reactivity of 1,2-DCB. At 500 °C, the chlorine equilibrium rates of the Pd–Ni and Ni catalysts reached 99%, while that of the Pd catalyst reached 94%. These results indicate that chlorine species did not fully reach 100% equilibrium on any of the catalysts, which may be attributed to slight chlorine retention on the catalyst surface or the formation of polychlorinated organic by-products.

The organic by-products formed during 1,2-DCB hydrolytic oxidation over different catalysts are presented in Fig. 3, which were identified as benzene, CB and 1,3-dichlorobenzene (1,3-DCB), with benzene as the dominant component. Reaction temperature exerted a critical effect on the formation of chlorinated organic by-products. For all three catalysts, the benzene yield exhibited a distinct rise-and-fall trend with increasing reaction temperature, yet the temperatures corresponding to the maximum benzene concentration differed among the catalyst systems: 450 °C was recorded for 0.5% Pd/ZSM-5(25), whereas both 10% Ni/ZSM-5(25) and 0.5% Pd–10% Ni/ZSM-5(25) reached their respective maxima at 400 °C. CB was detected across the full temperature range over 0.5% Pd/ZSM-

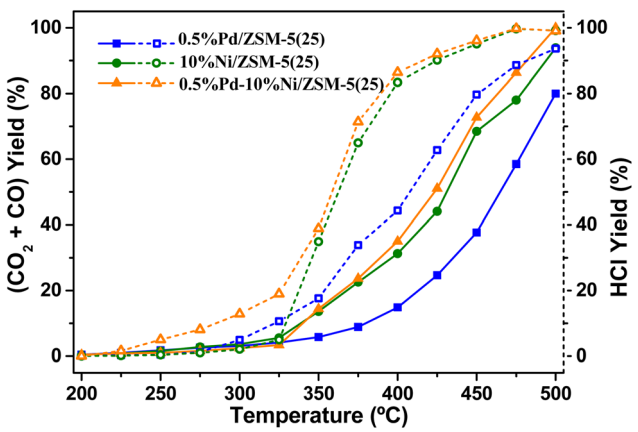

Fig. 2 Variation of CO_x yield (left vertical axis) and HCl yield (right vertical axis) with temperature during hydrolytic oxidation of 1,2-DCB.

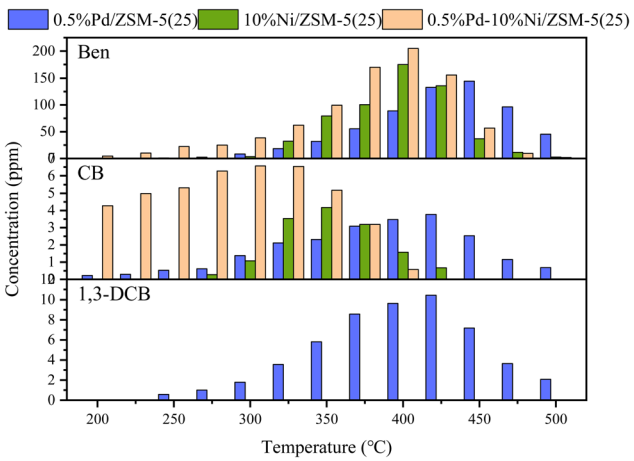

Fig. 3 Distribution of organic by-products in the hydrolytic oxidation of 1,2-DCB.

5(25), peaking at 3.8 ppm at 425 °C; over 10% Ni/ZSM-5(25), it only formed within 275–425 °C. For 0.5% Pd–10% Ni/ZSM-5(25), CB yield was higher, reaching a maximum of 6.6 ppm at 300 °C within 200–400 °C and undetectable at higher temperatures. Notably, 1,3-DCB was only detected over 0.5% Pd/ZSM-5(25), with its concentration rising then falling and peaking at 10.5 ppm at 425 °C, while no 1,3-DCB was found over the other two catalysts.

3.2 CB catalytic degradation activity and product distribution

In the previous section, it was shown that the 0.5% Pd–10% Ni/ZSM-5(25) catalyst was the most active catalyst for the hydrolytic oxidation of 500 ppm 1,2-DCB under the reaction conditions of 3.2 vol% H_2O and had a strong selectivity for the generation of HCl. To further investigate the catalytic oxidation performance of the three catalysts on CVOCs, 500 ppm CB was selected as the target compound under the same conditions, and the catalytic performance was determined.

The hydrolytic oxidation activity curves of the three catalysts for CB are shown in Fig. 4. The characteristic activity data for the reaction temperatures at 10%, 50% and 90% CB conversion are shown in Table 2. As can be seen from the Fig. 4, except for 0.5% Pd/ZSM-5(25), 10% Ni/ZSM-5(25) and 0.5% Pd–10% Ni/ZSM-5(25) catalysts can make the conversion of CB reach 100%, and the reaction temperatures required to realize complete conversion are 425 and 400 °C, respectively. Under the same reaction conditions, the 0.5% Pd–10% Ni/ZSM-5(25) catalyst exhibited the best catalytic activity for CB, and the temperature required to achieve 90% conversion ($T_{90\%}$ of 340 °C) was lower than that of 0.5% Pd/ZSM-5(25) and 10% Ni/ZSM-5(25) ($T_{90\%}$ of 417 and 363 °C, respectively).

As shown in Table 2, 0.5% Pd–10% Ni/ZSM-5(25) exhibits the best performance: its reaction rate at 200 °C (2.55 mmol g^{-1} s^{-1}) is the highest among the three catalysts, while its activation energy (38.3 kJ mol^{-1}) is the lowest, demonstrating stronger low-temperature reaction activity and catalytic efficiency. The reaction rate (0.80 mmol g^{-1} s^{-1}) and activation energy (69.1 kJ mol^{-1}) of 0.5% Pd/ZSM-5(25) are at a moderate level. In contrast, 10% Ni/ZSM-5(25) shows the lowest reaction rate (0.51 mmol g^{-1} s^{-1}) and the highest activation energy (104.3 kJ mol^{-1}), resulting in the weakest overall catalytic performance. The conversions increased with increasing temperature in the reaction temperature range. The CB conversions of the three catalysts were in the following order: 0.5% Pd–10% Ni/ZSM-5(25) > 10% Ni/ZSM-5(25) > 0.5% Pd/ZSM-5(25). Similarly, at low temperatures, the activity of the 10% Ni/ZSM-5(25) catalyst is lower than that of 0.5% Pd/ZSM-5(25).

The distribution of inorganic products (CO, CO_2 and HCl) in the hydrolytic oxidation of CB at different reaction temperatures is shown in Fig. 5 and S2. As can be seen from the Fig. S2, the CO yield was much higher than the CO_2 yield in the experimental temperature range. In the temperature interval of 100–200 °C, the CO production rate is extremely low, and then the CO production rate increases with the increase of temperature. When the temperature reached 325 °C, the CO_2 production rate began to increase. At 400 °C, the CO production rate of 10% Ni/ZSM-5(25) and 0.5% Pd/ZSM-5(25) catalysts started to slow down, while CO_2 still increased at a certain rate. At 450 °C, the CO and CO_2 yields of the three catalysts were: 0.5% Pd–10% Ni/ZSM-5(25) > 10% Ni/ZSM-5(25) > 0.5% Pd/ZSM-5(25).

At 450 °C, the three catalysts exhibit a distinct difference in CO_x selectivity: the CO_x selectivity of 0.5% Pd–10% Ni/ZSM-5(25) reaches 100%, enabling the complete mineralization of the target pollutant; the CO_x selectivity of 10% Ni/ZSM-5(25) is 94%, corresponding to a relatively high mineralization degree; in contrast, the CO_x selectivity of 0.5% Pd/ZSM-5(25) is only 80%, indicating a relatively weak mineralization performance.

At 100–150 °C, almost no HCl was generated during the hydrolytic oxidation of CB. At temperatures above 150 °C, the HCl concentration exhibited a monotonic increase with rising reaction temperature. As the temperature increased to 450 °C, the chlorine equilibrium rates of both 0.5% Pd–10% Ni/ZSM-5(25) and 10% Ni/ZSM-5(25) catalysts reach 99%, while that of

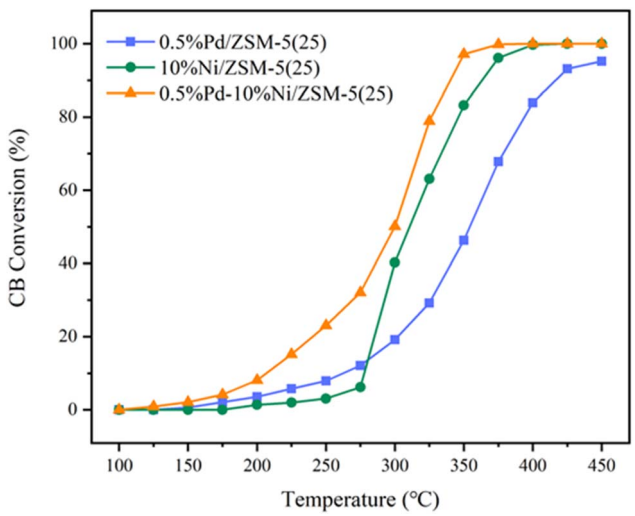

Fig. 4 CB hydrolytic oxidation activity curve.

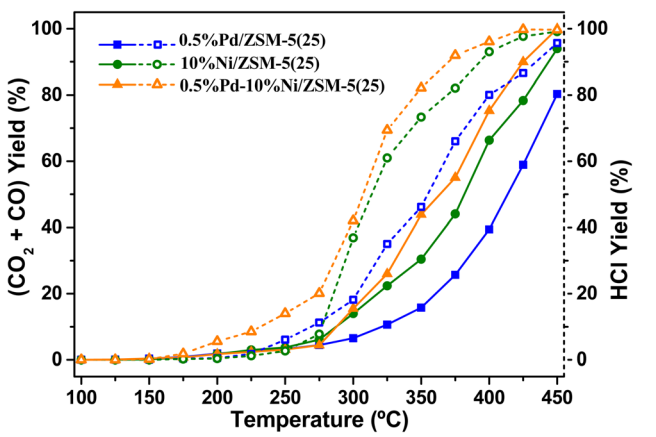

Fig. 5 Variation of CO_x yield (left vertical axis) and HCl yield (right vertical axis) with temperature during hydrolytic oxidation of CB.

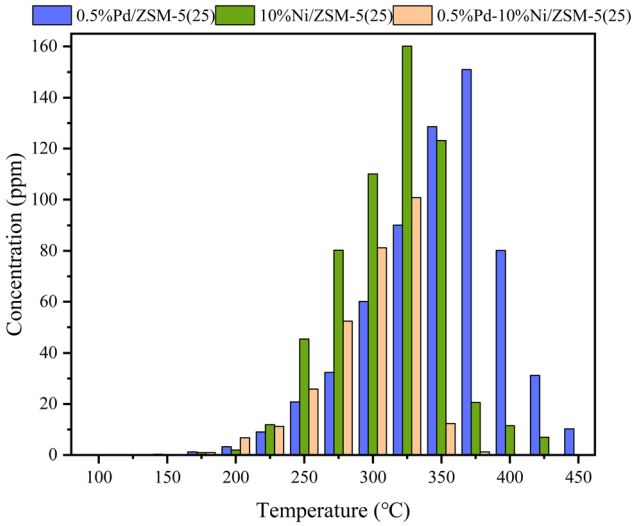

Fig. 6 Variation of benzene distribution with temperature during hydrolytic oxidation of CB.

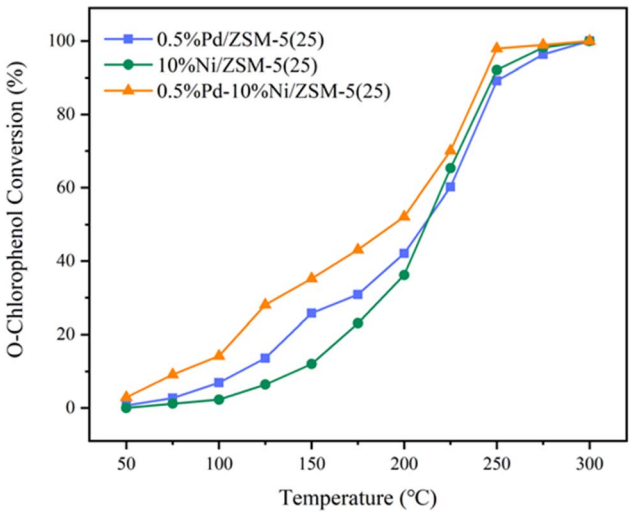

Fig. 7 Hydrolytic oxidation activity curves for *o*-chlorophenol.

0.5% Pd/ZSM-5(25) catalyst is 96%. 10% Ni/ZSM-5(25) and 0.5% Pd–10% Ni/ZSM-5(25), which means that only a very small amount of precipitation of chlorine species was formed on the catalyst surface or a small amount of polychlorinated organic by-products were formed. In addition, compared to the two catalysts, 0.5% Pd/ZSM-5(25) and 10% Ni/ZSM-5(25), 0.5% Pd–10% Ni/ZSM-5(25) exhibited a strong selectivity for HCl generation.

The distribution of organic by-products from CB hydrolytic oxidation is presented in Fig. 6. Benzene was identified as the sole by-product, with no other chlorinated organic by-products detected. No benzene was formed over the three catalysts at low temperatures (100–150 °C). Above this temperature range, the benzene concentration first increased and then decreased with elevating reaction temperature, with the peak concentration occurring at 375 °C for 0.5% Pd/ZSM-5(25) and at 325 °C for both 10% Ni/ZSM-5(25) and 0.5% Pd–10% Ni/ZSM-5(25). Benzene was no longer detectable at 400 °C over the 0.5% Pd–10% Ni/ZSM-5(25) catalyst, whereas the temperature required to achieve undetectable benzene levels was 450 °C over the 10% Ni/ZSM-5(25) catalyst. Overall, compared with the other two catalysts, 0.5% Pd–10% Ni/ZSM-5(25) exhibited lower organic by-product concentrations and higher reaction rates in CB hydrolytic oxidation.

3.3 Catalytic degradation activity and product distribution of *o*-chlorophenol

The activity of the hydrolytic oxidation reaction of 500 ppm *o*-chlorophenol was tested on 0.5% Pd/ZSM-5(25), 10% Ni/ZSM-5(25) and 0.5% Pd–10% Ni/ZSM-5(25) under reaction conditions of 3.2 vol% H_2O. The conversion curves are shown in Fig. 7, the conversion of *o*-chlorophenol increased with increasing temperature. As shown in Table 3, the reaction performances of the three catalysts show significant differences: 0.5% Pd–10% Ni/ZSM-5(25) exhibits the best performance, with a reaction rate of 2.69 mmol g^{-1} s^{-1} (the highest among the three) and an activation energy of only 28.3 kJ mol^{-1} (the lowest among the three), demonstrating superior low-temperature catalytic activity and reaction efficiency. The reaction rate (0.65 mmol g^{-1} s^{-1}) and activation energy (58.7 kJ mol^{-1}) of 0.5% Pd/ZSM-5(25) are at a moderate level. For 10% Ni/ZSM-5(25), it has the lowest reaction rate (0.52 mmol g^{-1} s^{-1}) and the highest activation energy (98.6 kJ mol^{-1}), resulting in the weakest overall catalytic performance. At temperatures up to 300 °C, complete conversion of *o*-chlorophenol was achieved with all three catalysts. Among them, the lowest temperature required for 90% conversion of 0.5% Pd–10% Ni/ZSM-5(25) was 243 °C, and the hydrolytic oxidation activity was the highest. Similarly, at low temperatures, the activity of 10% Ni/ZSM-5(25) catalyst was lower than that of 0.5% Pd/ZSM-5(25).

The inorganic product distribution from *o*-chlorophenol hydrolytic oxidation is shown in Fig. 8 and S3. Over 10% Ni/ZSM-5(25) and 0.5% Pd–10% Ni/ZSM-5(25), CO yield exceeded that of CO_2 throughout the tested temperature range; by contrast, CO and CO_2 yields were comparable over 0.5% Pd/ZSM-5(25). With rising temperature, CO yield increased then declined, while CO_2 yield rose steadily. CO yield peaked at 250 °C for all catalysts, reaching 54%, 67% and 74% for 0.5% Pd/ZSM-5(25), 10% Ni/ZSM-5(25) and 0.5% Pd–10% Ni/ZSM-5(25), respectively. Beyond this temperature, CO yield decreased continuously, with the most significant drop observed over 0.5% Pd–10% Ni/ZSM-5(25). At 300 °C, the CO_x selectivity of all catalysts can reach 100%, achieving the complete mineralization of the target pollutants.

Within the temperature range of 50–300 °C, the HCl concentration exhibited a monotonic increase with elevating reaction temperature. At 50 °C, 0.5% Pd/ZSM-5(25) and 10% Ni/ZSM-5(25) did not generate HCl, while 0.5% Pd–10% Ni/ZSM-5(25) had generated a small amount of HCl, which was consistent with the activity curve of *o*-chlorophenol. At 300 °C, the chlorine equilibrium rates of both 0.5% Pd–10% Ni/ZSM-

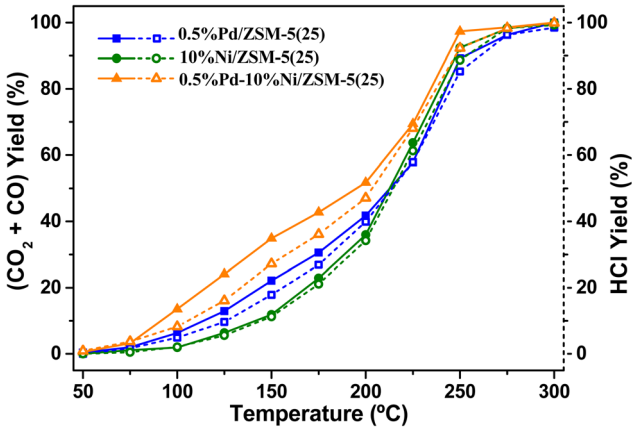

Fig. 8 Variation of CO_x yield (left vertical axis) and HCl yield (right vertical axis) with temperature during hydrolytic oxidation of *o*-chlorophenol.

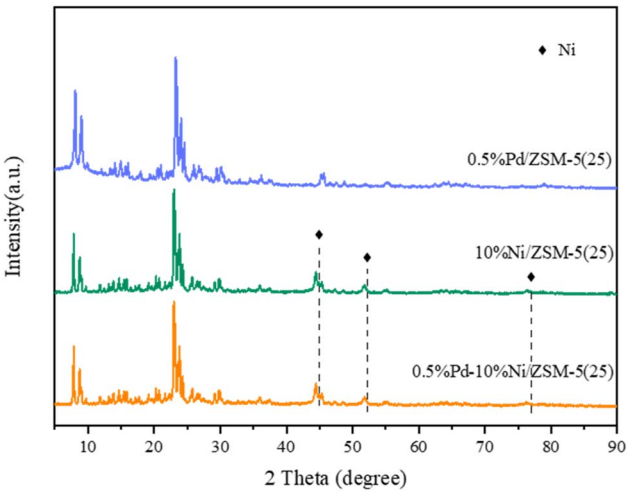

Fig. 9 XRD patterns of different catalysts.

5(25) and 10% Ni/ZSM-5(25) catalysts reach 99%. In contrast, the chlorine equilibrium rate of 0.5% Pd/ZSM-5(25) catalyst is 98%. The chlorine equilibrium rates over all catalysts reached 98–99% under the tested conditions, indicating that the chlorine balance approached but did not fully reach 100%. This slight discrepancy suggests that a small fraction of chlorine (approximately 1–2%) may exist in unmeasured forms, such as adsorbed chlorine species on the catalyst surface or trace amounts of undetected chlorinated organic by-products.

In summary, the order of temperatures required for the complete catalytic degradation of the three CVOCs is 1,2-DCB > CB > *o*-chlorophenol. This likely stems from differences in molecular structure and chemical bonding. The *o*-chlorophenol has OH groups, which increase its molecular polarity. Polar molecules more easily interact with polar substances in the environment, thus promoting degradation. The OH group in *o*-chlorophenol donates electrons, increasing the benzene-ring's electron-cloud density. This makes *o*-chlorophenol's chemical bonds more vulnerable to attack and breakage.

In contrast, CB is less polar, making it harder to interact with its surroundings and more difficult to degrade, so it needs higher temperatures. CB has a more stable electron-cloud distribution, requiring more energy to start degradation. In 1,2-DCB, two chlorine atoms on the benzene ring change the molecule's electron-cloud density, strengthening intermolecular forces. Dichlorobenzene has two C–Cl bonds with high combined bond energy, necessitating more energy to break them, hence a higher degradation temperature.

Nevertheless, despite the differences in the degradation temperatures required for the three target pollutants, the three catalysts exhibited comparable overall catalytic performance. Specifically, the low-temperature activity followed the sequence: 0.5% Pd–10% Ni/ZSM-5(25) > 0.5% Pd/ZSM-5(25) > 10% Ni/ZSM-5(25). In contrast, the activity ranking for achieving complete pollutant conversion was 0.5% Pd–10% Ni/ZSM-5(25) > 10% Ni/ZSM-5(25) > 0.5% Pd/ZSM-5(25). This divergence in activity trends is presumably associated with the intrinsic physicochemical properties of the catalyst surfaces.

3.4 Catalyst XRD analysis

Fig. 9 shows the XRD patterns of different catalysts in the range of 5–90° for 2θ. The characteristic ZSM-5 diffraction peaks appeared for all three catalysts, which indicated that the catalyst carriers still maintained the ZSM-5(25) zeolite molecular sieve structure after loading Pd and Ni metals. The diffraction peaks of Pd were not detected in the 0.5% Pd/ZSM-5(25) and 0.5% Pd–10% Ni/ZSM-5(25) catalysts, which was mainly due to the low Pd loading and the high dispersion of Pd on the surfaces of these two catalysts. In the XRD patterns of 10% Ni/ZSM-5(25) and 0.5% Pd–10% Ni/ZSM-5(25) catalysts, more obvious diffraction peaks of Ni existed at 2θ of 45.0, 52.2, and 77.1°,[33,34] and diffraction peaks of oxide NiO_2 were not detected[35] indicating that the active component existed on the surface of the catalysts in the form of amorphous or highly dispersed was achieved.

Fig. 10 shows the nitrogen adsorption–desorption isotherms measured at −196 °C. According to the classification standards of the International Union of Pure and Applied Chemistry (IUPAC), all ZSM-5 series catalysts exhibit type I isotherm characteristics, with an adsorption plateau observed at relatively high pressures and no obvious hysteresis loop. This indicates that all catalyst samples possess a microporous structure with an extremely low mesopore content. This conclusion is further corroborated by the pore structure parameters presented in Table 4—the data show that 70–80% of the total pore volume of each sample is contributed by micropores. Notably, the isotherms of the ZSM-5 catalysts show an upward trend in adsorption capacity when the relative pressure P/P_0 > 0.9, implying the possible presence of mesoporous structures in the catalysts.

The BET specific surface area of 0.5% Pd/ZSM-5(25) reaches 367 $m^2\ g^{-1}$, which is much higher than that of 10% Ni/ZSM-5(25) (297 $m^2\ g^{-1}$) and the bimetallic catalyst 0.5% Pd–10% Ni/ZSM-5(25) (292 $m^2\ g^{-1}$). This indicates that Pd monometallic modification causes less damage to the surface structure of the ZSM-5 support. In contrast, both Ni monometallic loading and Pd–Ni bimetallic co-loading lead to a significant decrease in the catalyst's specific surface area, and the specific surface area of

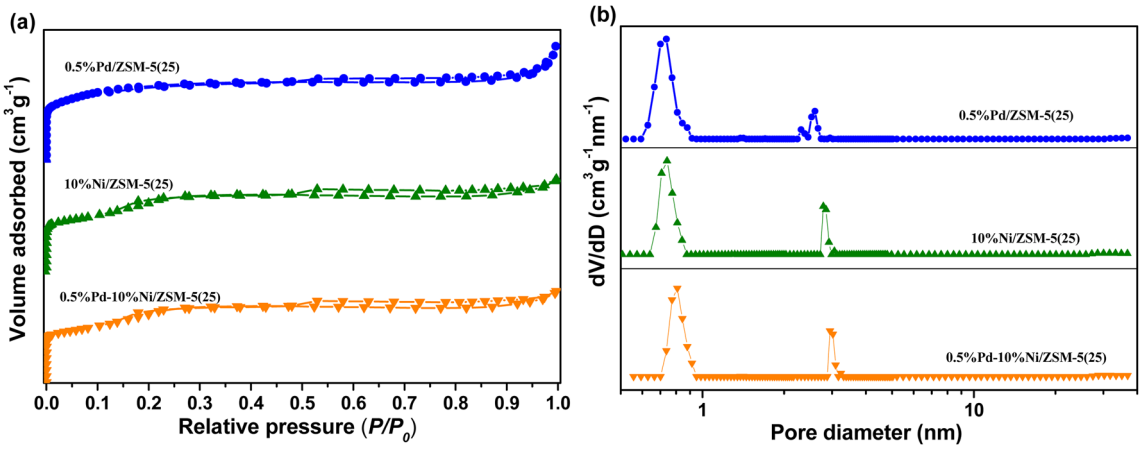

Fig. 10 (a) N_2 adsorption–desorption isotherms at −196 °C and (b) pore-size distributions evaluated from nitrogen physical adsorption of Pd/γ-Al_2O_3, Pd/ZSM-5(25), Pd/ZSM-5(200) and Pd/SiO_2.

the bimetallic catalyst is slightly lower than that of the Ni monometallic catalyst. It is inferred that Ni loading (especially bimetallic co-loading) tends to cause agglomeration or blockage of metal particles in the pores of ZSM-5, thereby reducing the effective specific surface area of the support.

3.5 Analysis of catalyst surface acidity

The infrared spectral analysis of the catalyst surface is shown in Fig. 11. The inverted peak at 1641 cm^{-1} corresponds to the bending vibration of the hydroxyl group in water.[36] The peak at 3607 cm^{-1} is due to the bridging hydroxyl group (Si–OH–Al) attributed to the Brønsted acid site,[37] as can be seen in the Fig. 11, 0.5% Pd/ZSM-5(25) > 10% Ni/ZSM-5(25) > 0.5% Pd–10% Ni/ZSM-5(25). For the 0.5% Pd/ZSM-5(25) catalyst, the distinct absorption peak detected at 3737 cm^{-1} corresponds to the free external hydroxyl groups on the zeolite surface.[38,39] In contrast to the 10% Ni/ZSM-5(25), the absorption peak at 3737 cm^{-1} was weaker, and the absorption peak corresponding to 0.5% Pd–10% Ni/ZSM-5(25) was in between, from which it can be hypothesized that the loading of Ni would inhibit hydroxyl generation, and that the catalytic performance of the catalysts can be optimized by controlling the Pd–Ni ratio.

In order to further investigate the effect of the loaded metal species on the catalyst performance, the surface acidity of the three catalysts was investigated using pyridine FTIR spectroscopy, and the results are shown in Fig. 12. The FTIR peaks at 1450 cm^{-1} and 1540 cm^{-1} are attributed to Lewis and Brønsted acidic sites, respectively, while the FTIR peak at 1490 cm^{-1} is the sum of Brønsted and Lewis acidic sites.[40,41] Combined with the data in Fig. 12 and Table 5, it can be seen that 0.5% Pd/ZSM-5(25) exhibits the largest number of acidic sites and the strongest total acidity compared with 10% Ni/ZSM-5(25) and 0.5% Pd–10% Ni/ZSM-5(25). In contrast, although 0.5% Pd–10% Ni/ZSM-5(25) has the lowest total acidity among the three catalysts (with a relative total acidity of only 0.41), its Brønsted/Lewis (B/L) acid ratio reaches the highest value of 4.16. Further correlation analysis between the catalytic activity and the Brønsted/Lewis (B/L) acid ratio, when combined with the

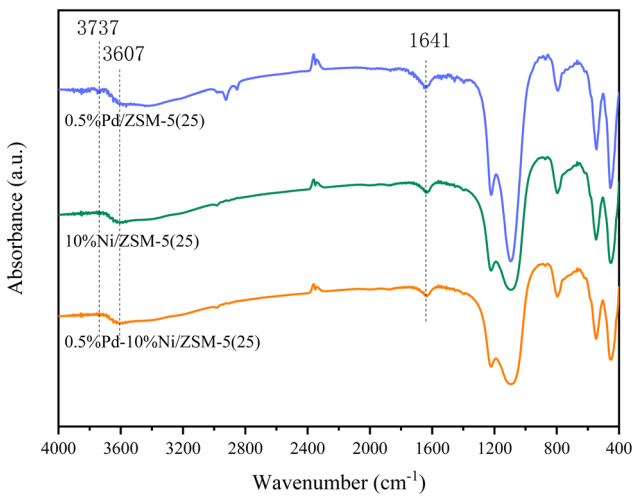

Fig. 11 FTIR spectra on different catalysts.

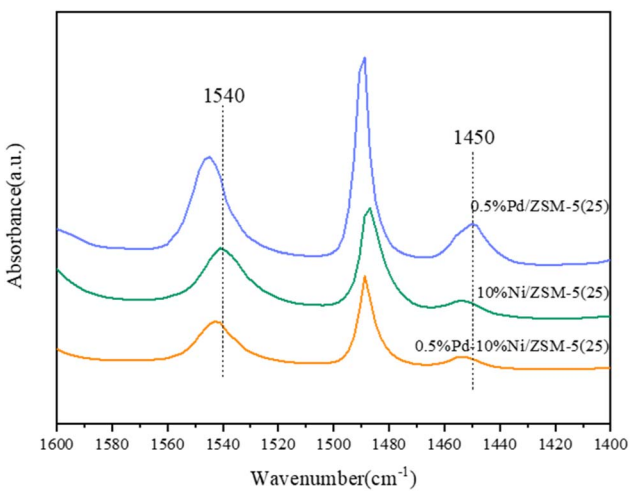

Fig. 12 Infrared spectrum of pyridine adsorption on different catalysts.

activity test results for *o*-chlorophenol (as illustrated in Fig. 7), reveals a distinct positive correlation between these two parameters.

It is evident that metal loading exerts a dual regulatory effect on the acidic properties of the catalysts. On the one hand, an increase in metal loading results in the coverage of partial acid sites on the catalyst surface, thereby inducing a gradual reduction in the total acid content. For instance, the relative total acidity decreases progressively from 0.87 (0.5% Pd/ZSM-5(25)) to 0.50 (10% Ni/ZSM-5(25)) and finally to 0.41 (0.5% Pd–10% Ni/ZSM-5(25)). On the other hand, the introduction of Ni significantly enhances the relative proportion of Brønsted acid sites. This structural feature enables the bimetallic catalyst to maintain favorable reaction activity by virtue of its high B/L acid ratio, even under the condition of low total acidity.

It has been reported in the literature that Lewis acidic sites contribute to the adsorption of H_2O, chlorine-containing organic compounds on the surface of the catalysts.[42] H_2O engages in free–radical reactions during the reaction course. Specifically, H_2O can interact with chlorine radicals (Cl˙). When Cl˙ attacks the H_2O molecule, the O–H bond therein ruptures. Cl˙ abstracts a hydrogen atom from H_2O, yielding hydrogen chloride (HCl) and hydroxyl radicals (˙OH). The corresponding reaction equation is presented as: $Cl^{\cdot} + H_2O \rightarrow HCl + {}^{\cdot}OH$. Significantly, the generated ˙OH, being a substantially more potent oxidizing agent, will subsequently react with CVOCs.

Moreover, the Brønsted acidic sites are capable of engaging in interactions with reactant molecules through the donation of protons, leading to the protonation of the reactant molecules. This protonation event modifies the electron cloud distribution within the molecules, thereby decreasing the activation energy of the reaction. Consequently, the reactant molecules become more amenable to oxidation by oxidizing agents. During the course of the reaction, Brønsted acidic sites induce the protonation of pollutant molecules, augmenting the polarity of chemical bonds such as C–C, C–H, and O–H within these molecules. This enhanced polarity renders these chemical bonds more prone to cleavage, thereby facilitating the advancement of the oxidation reaction.[43–46] Brønsted acidic sites can participate in the redox cycling process of the catalyst. These species can modulate the electron density and oxidation states of active sites on the catalyst surface, thereby exerting a pronounced influence on the catalytic activity and long-term stability of the catalyst system.

This also indicates that the catalytic activity of the 0.5% Pd/ZSM-5(25) catalyst is higher than that of the 10% Ni/ZSM-5(25) catalyst at low temperatures. However, the 0.5% Pd–10% Ni/ZSM-5(25) catalyst exhibits the weakest acidity but the strongest activity, which is likely related to the water species adsorbed on the catalyst surface.

3.6 Water species adsorbed on the catalyst surface

To further investigate the effect of water protonation in the hydrolytic oxidation, TPD was used to characterize the different adsorbed water forms of the catalysts. The H_2O-TPD curves are shown in Fig. 13. The H_2O-TPD curves were applied to the

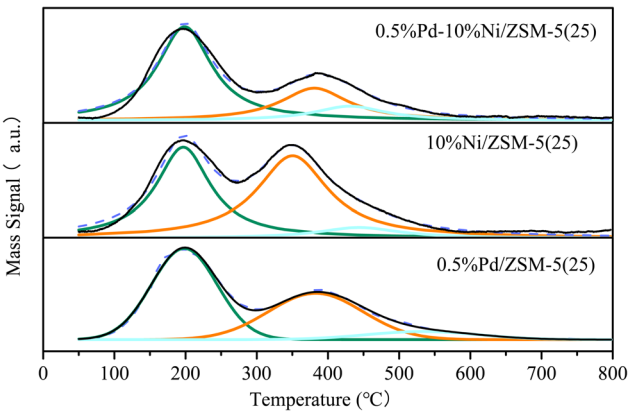

Fig. 13 The H_2O-TPD profiles of each catalyst.

Lorentz equation. For 0.5% Pd/ZSM-5(25), 10% Ni/ZSM-5(25) and 0.5% Pd–10% Ni/ZSM-5(25), three H_2O desorption peaks appeared at 50–800 °C. The first desorption peak belongs to the type I water, which is characterized by no interaction with the catalyst surface. The second peak belongs to type II water, which can be attributed to the interaction between the surface and adsorbed water or hydroxide through hydrogen bonding. The third peak belongs to type III water, which is mainly due to the strong adsorption of water on the catalyst surface. Wang *et al.*[47] demonstrated that in the hydrolysis reaction, only type III water can supply the active protons necessary for the reaction. As illustrated in the graph, compared with the other two Ni-containing catalysts, the desorption of type III water on 0.5% Pd/ZSM-5(25) demands a relatively higher temperature. The intensity sequence of type III water is as follows: 0.5% Pd–10% Ni/ZSM-5(25) > 10% Ni/ZSM-5(25) > 0.5% Pd/ZSM-5(25). This phenomenon is in line with the order of hydrolytic oxidation activity of the catalyst towards various chlorinated pollutants.

3.7 Catalyst XPS analysis

The Ni 2p spectra were determined by XPS as in Fig. 14. For the 0.5% Pd–10% Ni/ZSM-5(25) catalyst, the Ni $2p_{1/2}$ binding energy

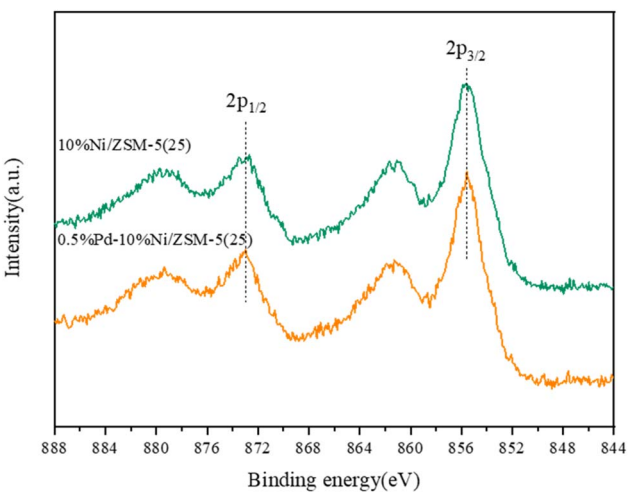

Fig. 14 Ni 2p XPS spectra for different catalysts.

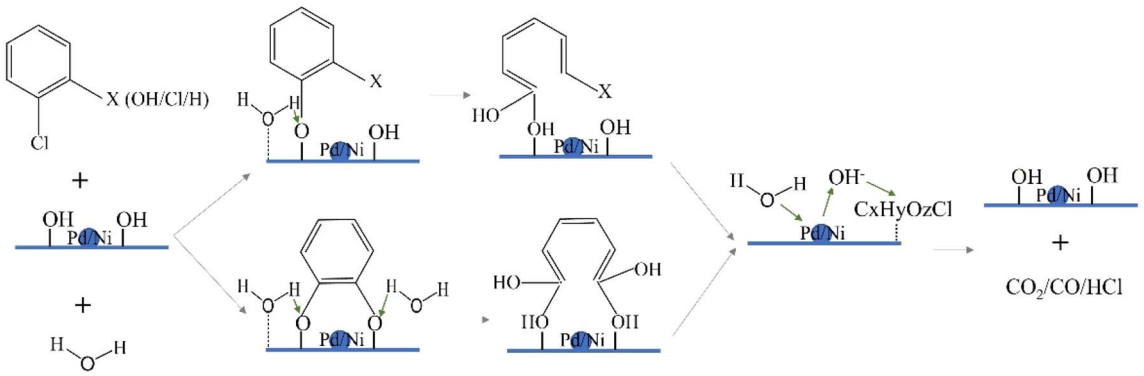

Scheme 1 The hydrolytic oxidation mechanism of CVOCs on the catalyst surface.

is clearly observed around 873 eV, which can be attributed to Ni^{2+} in NiO, whereas the binding energy at 855.6 eV corresponds to Ni^{2+} $2p_{3/2}$. As can be seen from the Fig. 14, the binding energy of 10% Ni/ZSM-5(25) is shifted to a lower position at Ni $2p_{1/2}$ and its peak intensity corresponding to Ni^{2+} $2p_{3/2}$ is slightly weaker as compared to that of 0.5% Pd–10% Ni/ZSM-5(25) catalyst. Therefore, the higher the Ni 2p binding energy of the 0.5% Pd–10% Ni/ZSM-5(25) catalyst, the higher the positive charge of Ni and its redox capacity. The high redox performance of Ni enables it to more effectively adsorb and activate reactive molecules. In the hydrolytic oxidation reaction, after water molecules are adsorbed on the Ni surface, they are activated into highly reactive hydroxyl species through a redox process. These surface-active hydroxyl groups are capable of rapidly reacting with the target reactant molecules, thereby accelerating the overall reaction rate of the catalytic process.

Based on the results of the above studies combined with relevant literature reports, we hypothesize that the hydrolytic oxidation of CVOCs proceeds through the Langmuir–Hinshelwood mechanism. As shown in Scheme 1, it can be inferred from previous research and literature evidence[24,25] that CVOCs molecules, with their electron-donating chlorine substituents, tend to adsorb onto Lewis acid sites that are capable of accepting electrons. Subsequently, as supported by the findings of ref. 48 and 49, the C–Cl bond is subjected to nucleophilic attack by the oxygen atom of the hydroxyl (OH) group, leading to

Table 1 For the hydrolytic oxidation of 1,2-DCB, catalytic activity and kinetic parameters

Catalysts	$T_{10\%}$ (°C)	$T_{50\%}$ (°C)	$T_{90\%}$ (°C)	$r_{1,2\text{-DCB}}{}^{a}$ (mmol g^{-1} s^{-1})	$E_a{}^{b}$ (kJ mol^{-1})
0.5% Pd/ZSM-5(25)	324	408	469	0.98	67.8
10% Ni/ZSM-5(25)	328	358	397	0.52	103.2
0.5% Pd–10% Ni/ZSM-5(25)	265	351	394	2.44	44.3

[a] Calculated at 250 °C. [b] Measured when the conversion of 1,2-DCB was <15%.

Table 2 For the hydrolytic oxidation of CB, catalytic activity and kinetic parameters

Catalysts	$T_{10\%}$ (°C)	$T_{50\%}$ (°C)	$T_{90\%}$ (°C)	$r_{1,2\text{-DCB}}{}^{a}$ (mmol g^{-1} s^{-1})	$E_a{}^{b}$ (kJ mol^{-1})
0.5% Pd/ZSM-5(25)	263	354	417	0.80	69.1
10% Ni/ZSM-5(25)	278	311	363	0.51	104.3
0.5% Pd–10% Ni/ZSM-5(25)	202	300	340	2.55	38.3

[a] Calculated at 200 °C. [b] Measured when the conversion of CB was <15%.

Table 3 For the hydrolytic oxidation of *o*-chlorophenol, catalytic activity and kinetic parameters

Catalysts	$T_{10\%}$ (°C)	$T_{50\%}$ (°C)	$T_{90\%}$ (°C)	$r_{1,2\text{-DCB}}{}^{a}$ (mmol g^{-1} s^{-1})	$E_a{}^{b}$ (kJ mol^{-1})
0.5% Pd/ZSM-5(25)	112	211	253	0.65	58.7
10% Ni/ZSM-5(25)	141	212	248	0.52	98.6
0.5% Pd–10% Ni/ZSM-5(25)	79	194	243	2.69	28.3

[a] Calculated at 75 °C. [b] Measured when the conversion of *o*-chlorophenol was <15%.

Table 4 Textural properties of catalysts

Catalyst	S_{BET}[a] (m^2 g^{-1})	Pore volume (cm^3 g^{-1})		Pore size[d] (nm)
		Micropore[b]	Total[c]	
0.5% Pd/ZSM-5(25)	367	0.15	0.21	0.7/2.6
10% Ni/ZSM-5(25)	297	0.11	0.17	0.8/2.8
0.5% Pd–10% Ni/ZSM-5(25)	292	0.10	0.17	0.8/2.8

[a] BET specific surface areas determined from the linear part of the BET equation (P/P_0 = 0.05–0.25). [b] *t*-Plot micropore volumes. [c] Total pore volumes obtained at P/P_0 = 0.99. [d] Pore diameter.

Table 5 Acidic properties of 0.5% Pd/ZSM-5(25), 10% Ni/ZSM-5(25), and 0.5% Pd–10% Ni/ZSM-5(25) catalysts measured by pyridine FTIR

Catalyst	C_B[a] (mmol g-cat.$^{-1}$)	C_L[b] (mmol g-cat.$^{-1}$)	Brønsted/Lewis acidity ratio	Relative total acidity[c]
0.5% Pd/ZSM-5(25)	1.62	0.47	3.45	0.87
10% Ni/ZSM-5(25)	0.96	0.25	3.84	0.50
0.5% Pd–10% Ni/ZSM-5(25)	0.79	0.19	4.16	0.41

[a] C(Brønsted) = 1.88 × I_A(B) × R^2/W. [b] C(Lewis) = 1.42 × I_A(L) × R^2/W, where I_A(B, L) = absorbance of Brønsted or Lewis acid sites; R = wafer radius (cm); W = catalyst mass (mg). [c] With the pristine ZSM-5 catalyst (without modification) as the reference.

the formation of surface-bound chlorophenol intermediates and semiquinone-type radicals. Based on a comprehensive analysis of our experimental data combined with relevant published literature, these generated reaction intermediates are proposed to proceed through two distinct reaction pathways: (i) reacting with surface chlorine species to form polychlorinated organic by-products, and (ii) undergoing further oxidative degradation to achieve complete mineralization.

Based on the significant positive correlation between the catalytic activity and the Brønsted/Lewis (B/L) acid ratio of the catalysts, as evidenced by the experimental data in Tables 1 (2 and 3) and 5, we infer the following reaction mechanism: when a water molecule approaches the Brønsted acid site, the H^+ at the site interacts with the water molecule owing to the proton-donating property of Brønsted acid sites. Upon the transfer of a proton from the Brønsted acid site to the lone-pair electrons of the water molecule, a hydrated hydrogen ion (H_3O^+) is generated, following the reaction: $-BH^+ + H_2O \rightarrow -B + H_3O^+$. The formed H_3O^+ is unstable either on the catalyst surface or within the reaction system. On the surface of metal oxide catalysts, OH may combine with metal cations to form hydroxylated surface species while releasing H^+; this released H^+ can then react with chlorine atoms adsorbed on the catalyst surface to produce HCl, while simultaneously freeing up the adsorption sites on the catalyst surface. The above discussion precisely elucidates the intrinsic correlation between type III water concentration and the decomposition activity of the catalyst, as shown in Fig. 13. Meanwhile, H_3O^+ can lead to the secondary protonation of chlorophenols or semiquinones intermediates, which in turn promotes the cleavage of the benzene ring C–C bonds and the formation of $C_xH_yO_z$ species.[50–52]

Based on XPS characterization results, the Ni species in the 0.5% Pd–10% Ni/ZSM-5(25) catalyst exhibit prominent redox capability. Meanwhile, experimental data (as presented in Fig. 1, 4, or 7) have further confirmed that this catalyst possesses excellent activity toward the hydrolytic oxidation of CVOCs. On this basis, we propose the following reaction mechanism speculation: the Ni-based active sites on the surface of 0.5% Pd–10% Ni/ZSM-5(25) can efficiently adsorb the *in situ* generated intermediate species and H_2O molecules during the reaction. Specifically, the C–H bonds in these intermediate species undergo dissociation under the catalytic action of the Ni surface, leading to the formation of adsorbed intermediates. Concurrently, H_2O molecules undergo dissociative adsorption on the Ni surface to produce active hydroxyl species, which subsequently oxidize the aforementioned adsorbed intermediates into CO and CO_2.

4 Conclusion

A comparative study of hydrolytic oxidation for 1,2-DCB, CB and *o*-chlorophenol over the same catalysts revealed that pollutant type exerts a critical impact on catalytic performance. Specifically, the $T_{90\%}$ values followed the order: *o*-chlorophenol < CB < 1,2-DCB, which was primarily ascribed to the differences in molecular structure and chemical bonding of the pollutants. Across all tested pollutants, the 0.5% Pd–10% Ni/ZSM-5(25) catalyst exhibited optimal catalytic activity. The bimetallic Pd–Ni catalyst outperformed the monometallic Pd and Ni counterparts significantly, a phenomenon mainly attributable to its enhanced surface acidity, abundant active protons and superior redox properties. However, the catalyst exhibits poor stability in the hydrolytic oxidation of CVOCs, and long-term operational stability remains a core challenge restricting its practical application. Therefore, further modification and regulation strategies (such as doping anti-coking functional additives, optimizing the microstructure and surface properties of the support, *etc.*) are required to enhance the long-term operational

durability of the catalyst, thereby meeting the practical application requirements in industrial scenarios. In conclusion, these findings provide valuable insights for the advancement of catalytic materials and eco-friendly technologies targeting CVOC elimination.

Author contributions

Formal analysis, Wenjie Song, Caifei Ni and Wenlong Fu; investigation, Jiahui Zhou and Zhen Han; writing – original draft, Yuqing Li, Bisi Lv and Na Li. All authors reviewed the manuscript.

Conflicts of interest

The authors declare no conflicts of interest.

Data availability

All data generated during the chemical experiments (including raw reaction yield data, catalyst characterization results such as XRD patterns, H_2O-TPD, and XPS spectra, as well as gas chromatography and on-line analysis by upper FTIR spectrometer analysis data of reaction products) and the detailed preparation protocols of materials (*e.g.*, the synthesis process of 0.5% Pd–10% Ni/ZSM-5 catalyst, reagent grades and suppliers) are publicly available to ensure experiment reproducibility.

Supplementary information (SI) is available. See DOI: https://doi.org/10.1039/d5ra08447d.

Acknowledgements

This project was funded by Natural Science Foundation of Shandong Province (ZR2021QB133). Thank you to all the teachers for their assistance during the characterization of catalytic materials.

References

1 Y. Su, K. Fu, C. Pang, *et al.*, Recent advances of chlorinated volatile organic compounds' oxidation catalyzed by multiple catalysts: Reasonable adjustment of acidity and redox properties, *Environ. Sci. Technol.*, 2022, **56**, 9854–9871.
2 H. Jia, Y. Xing, L. Zhang, *et al.*, Progress of catalytic oxidation of typical chlorined volatile organic compounds (CVOCs): A review, *Sci. Total Environ.*, 2023, **865**, 161063.
3 P. Wang, L. Wang, Y. Zhao, *et al.*, Progress in degradation of volatile organic compounds by catalytic oxidation: a review based on the kinds of active components of catalysts, *Water, Air, Soil Pollut.*, 2024, **235**, 7.
4 M. Ma, R. Albilali and C. He, Recent advancements and challenges in the catalytic purification of volatile organic compounds, *Environ. Sci.: Nano*, 2024, **11**, 4060–4073.
5 B. Chen, Y. Wen, S. Gao, *et al.*, Mechanistic insights into the role of acidity to activity and anti-poisoning over Nb based catalysts for CVOCs combustion, *Appl. Catal., A*, 2022, **636**, 118581.
6 C. He, J. Cheng, X. Zhang, *et al.*, Recent advances in the catalytic oxidation of volatile organic compounds: a review based on pollutant sorts and sources, *Chem. Rev.*, 2019, **119**, 4471–4568.
7 H. Liu, X. Li, Q. Dai, *et al.*, Catalytic oxidation of chlorinated volatile organic compounds over Mn-Ti composite oxides catalysts: Elucidating the influence of surface acidity, *Appl. Catal., B*, 2021, **282**, 119577.
8 J. Wang, F. Dong, Z. Tang, *et al.*, Insights into the Electronic structure effect of $SnMnO_x$ nanorod catalysts for low-temperature catalytic combustion of o-dichlorobenzene, *Chem.–Asian J.*, 2023, **18**, e202300413.
9 C. Li, Y. Zhao, H. Song, *et al.*, A review on recent advances in catalytic combustion of chlorinated volatile organic compounds, *J. Chem. Technol. Biotechnol.*, 2020, **95**, 2069–2082.
10 S. Ding, S. Wu, N. Fang, *et al.*, Recent advances in chlorinated volatile organic compounds' oxidation over multiple noble metal catalysts: A review based on rational manipulation of redox-acidity balance, *Sep. Purif. Technol.*, 2024, **349**(3), 127859.
11 X. Yan, L. Zhao, Y. Huang, *et al.*, Three-dimensional porous CuO-modified CeO_2-Al_2O_3 catalysts with chlorine resistance for simultaneous catalytic oxidation of chlorobenzene and mercury: Cu-Ce interaction and structure, *J. Hazard. Mater.*, 2023, **455**, 131585.
12 B. Xie, Z. Wei, M. Ding, *et al.*, Enhanced Ru-O-Ce interaction by solid solution structure of Ru-$Ce_xZr_{1-x}O_2$ catalysts for efficient catalytic combustion of vinyl chloride, *Appl. Catal., B: Environ. Energy*, 2024, **350**, 123926.
13 D. Xing, S. Wang, Y. Fan, *et al.*, Formation of PCDD/Fs, PCBs and HCl during catalytic combustion of chlorobenzene over supported transition metal (Cr, V and Cu) oxide catalysts, *J. Environ. Chem. Eng.*, 2023, **11**, 109267.
14 Y. Long, J. Liu, M. Chen, *et al.*, Catalytic destruction of chlorobenzene over K-OMS-2: Inhibition of high toxic byproducts via phosphate modification, *J. Environ. Sci.*, 2023, **127**, 844–854.
15 Y. Gu, T. Cai, X. Gao, *et al.*, Catalytic combustion of chlorinated aromatics over WO_x/CeO_2 catalysts at low temperature, *Appl. Catal., B*, 2019, **248**, 264–276.
16 X. Weng, P. Sun, Y. Long, *et al.*, Catalytic oxidation of chlorobenzene over $Mn_xCe_{1-x}O_2$/HZSM-5 catalysts: A study with practical implications, *Environ. Sci. Technol.*, 2017, **51**, 8057–8066.
17 P. Sun, W. Wang, X. Weng, *et al.*, Alkali potassium induced HCl/CO_2 selectivity enhancement and chlorination reaction inhibition for catalytic oxidation of chloroaromatics, *Environ. Sci. Technol.*, 2018, **52**, 6438–6447.
18 W. Deng, Q. Tang, S. Huang, *et al.*, Low temperature catalytic combustion of chlorobenzene over cobalt based mixed oxides derived from layered double hydroxides, *Appl. Catal., B*, 2020, **278**, 119336.
19 P. Wang, S. Ding, S. Wu, *et al.*, Investigation of the by-product selectivity of industrialized support for the catalytic elimination of *o*-DCB over Pt-catalysts, *Microporous Mesoporous Mater.*, 2025, **381**, 113334.

20 H. Zhang, X. Gao, B. Gong, *et al.*, Catalytic combustion of CVOCs over MoO_x/CeO_2 catalysts, *Appl. Catal., B*, 2022, **310**, 121240.

21 M. Tian, X. Guo, R. Dong, *et al.*, Insight into the boosted catalytic performance and chlorine resistance of nanosphere-like meso-macroporous $CrO_x/MnCo_3O_x$ for 1,2-dichloroethane destruction, *Appl. Catal., B*, 2019, **259**, 118018.

22 Q. Dai, S. Bai, J. Wang, *et al.*, The effect of TiO_2 doping on catalytic performances of Ru/CeO_2 catalysts during catalytic combustion of chlorobenzene, *Appl. Catal., B*, 2013, **142**, 222–233.

23 J.-M. Giraudon, T. Nguyen, G. Leclercq, *et al.*, Chlorobenzene total oxidation over palladium supported on ZrO_2, TiO_2 nanostructured supports, *Catal. Today*, 2008, **137**, 379–384.

24 N. Li, J. Cheng, X. Xing, *et al.*, Distribution and formation mechanisms of polychlorinated organic by-products upon the catalytic oxidation of 1, 2-dichlorobenzene with palladium-loaded catalysts, *J. Hazard. Mater.*, 2020, **393**, 122412.

25 N. Li, X. Xing, J. Cheng, *et al.*, Influence of oxygen and water content on the formation of polychlorinated organic by-products from catalytic degradation of 1,2-dichlorobenzene over a Pd/ZSM-5 catalyst, *J. Hazard. Mater.*, 2021, **403**, 123952.

26 S. Wu, X. Lv, X. Hao, *et al.*, Enhancement of mineralization ability and water resistance of vanadium-based catalysts for catalytic oxidation of chlorobenzene by platinum loading, *Environ. Sci. Technol.*, 2024, **58**, 15836–15845.

27 X. Lv, S. Wu, S. Shao, *et al.*, Efficient catalytic elimination of chlorobenzene based on the water vapor-promoting effect within Mn-based catalysts: Activity enhancement and polychlorinated byproduct inhibition, *Environ. Sci. Technol.*, 2024, **58**, 3985–3996.

28 X. Yu, L. Dai, Y. Peng, *et al.*, High selectivity to HCl for the catalytic removal of 1,2-dichloroethane Over RuP/3DOM WO_x: Insights into the effects of P-doping and H_2O introduction, *Environ. Sci. Technol.*, 2021, **55**, 14906–14916.

29 M. Xu, S. Yao, D. Rao, *et al.*, Insights into interfacial synergistic catalysis over $Ni@TiO_{2-x}$ catalyst toward water–gas shift reaction, *J. Am. Chem. Soc.*, 2018, **140**, 11241–11251.

30 M. Xu, S. He, H. Chen, *et al.*, TiO_{2-x}-modified Ni nanocatalyst with tunable metal–support interaction for water–gas shift reaction, *ACS Catal.*, 2017, **7**, 7600–7609.

31 A. A. Gonçalves, P. B. Faustino, J. M. Assaf, *et al.*, One-pot synthesis of mesoporous Ni–Ti–Al ternary oxides: highly active and selective catalysts for steam reforming of ethanol, *ACS Appl. Mater. Interfaces*, 2017, **9**, 6079–6092.

32 J. J. Plata, J. Graciani, J. Evans, *et al.*, Cu deposited on CeO_x-modified TiO_2(110): synergistic effects at the metal–oxide interface and the mechanism of the WGS reaction, *ACS Catal.*, 2016, **6**, 4608–4615.

33 Y. Su, C. Shu, C. Ding, *et al.*, Solid solution of $Ce_{1-x}Y_xO_{2-\delta}$ supported nickel-based catalysts for auto-thermal reforming of acetic acid with high resistance to coking, *J. Energy Inst.*, 2024, **114**, 101589.

34 B. Qu, Y. S. Zhang, T. Wang, *et al.*, Pyrolysis-catalysis of waste tire to enhance the aromatics selectivity via metal-modified ZSM-5 catalysts, *Process Saf. Environ. Prot.*, 2024, **190**, 138–148.

35 W. Fu, Y. W. Cheng, D. Xu, *et al.*, Reaction synergy of bimetallic catalysts on ZSM-5 support in tailoring plastic pyrolysis for hydrogen and value-added product production, *Appl. Energy*, 2024, **372**, 123853.

36 S. Wu, P. Wang, N. Fang, *et al.*, In-situ encapsulated CeO_2 and doped Al in meso-ZSM-5 for efficient catalytic combustion of *o*-dichlorobenzene, *Appl. Catal., B: Environ. Energy*, 2024, **358**, 124412.

37 Y. Yuan, E. Huang, S. Hwang, *et al.*, Confining platinum clusters in indium-modified ZSM-5 zeolite to promote propane dehydrogenation, *Nat. Commun.*, 2024, **15**, 6529.

38 R. Zhang, Z. Wen, C. Chai, *et al.*, Amine-free synthesis of high-silica ZSM-5 assisted with calcined silicalite-1 and ethanol with the investigation of mechanism, *Microporous Mesoporous Mater.*, 2024, **375**, 113160.

39 K. Badvi and V. Javanbakht, Enhanced photocatalytic degradation of dye contaminants with TiO_2 immobilized on ZSM-5 zeolite modified with nickel nanoparticles, *J. Cleaner Prod.*, 2021, **280**, 124518.

40 S. Yuanyuan, Z. Li, X. Zhou, *et al.*, Mesoporous zeolite ZSM-5 confined Cu nanoclusters for efficient selective catalytic reduction of NO_x by NH_3, *Appl. Catal., B: Environ. Energy*, 2024, **346**, 123747.

41 K. Chen, X. Wu, J. Zhao, *et al.*, Organic-free modulation of the framework Al distribution in ZSM-5 zeolite by magnesium participated synthesis and its impact on the catalytic cracking reaction of alkanes, *J. Catal.*, 2022, **413**, 735–750.

42 B. H. Aristizábal, C. M. de Correa, A. I. Serykh, *et al.*, In situ FTIR study of the adsorption and reaction of ortho-dichlorobenzene over Pd-promoted Co-HMOR, *Microporous Mesoporous Mater.*, 2008, **112**, 432–440.

43 Z. Li, R. Gao, Z. Hou, *et al.*, Tandem supported Pt and ZSM-5 catalyst with separated catalytic functions for promoting multicomponent VOCs oxidation, *Appl. Catal., B*, 2023, **339**, 123131.

44 A. Aranzabal, M. Romero-Sáez, U. Elizundia, *et al.*, Deactivation of H-zeolites during catalytic oxidation of trichloroethylene, *J. Catal.*, 2012, **296**, 165–174.

45 J. González-Velasco, R. López-Fonseca, A. Aranzabal, *et al.*, Evaluation of H-type zeolites in the destructive oxidation of chlorinated volatile organic compounds, *Appl. Catal., B*, 2000, **24**, 233–242.

46 P. Sun, W. Wang, X. Dai, *et al.*, Mechanism study on catalytic oxidation of chlorobenzene over $Mn_xCe_{1-x}O_2$/H-ZSM5 catalysts under dry and humid conditions, *Appl. Catal., B*, 2016, **198**, 389–397.

47 Y. Wang, F. Wang, Q. Song, *et al.*, Heterogeneous ceria catalyst with water-tolerant Lewis acidic sites for one-pot synthesis of 1,3-diols via Prins condensation and hydrolysis reactions, *J. Am. Chem. Soc.*, 2013, **135**, 1506–1515.

48 S. Lomnicki, H. Truong, E. Vejerano and B. Dellinger, Copper oxide-based model of persistent free radical

formation on combustion-derived particulate matter, *Environ. Sci. Technol.*, 2008, **42**, 4982–4988.

49 G. R. Farquar, S. Alderman, E. Poliakoff and B. Dellinger, X-ray spectroscopic studies of the high temperature reduction of Cu(II)O by 2-chlorophenol on a simulated fly ash surface, *Environ. Sci. Technol.*, 2003, **37**, 931–935.

50 P. Sun, W. Wang, X. Weng, *et al.*, Alkali potassium induced HCl/CO_2 selectivity enhancement and chlorination reaction inhibition for catalytic oxidation of chloroaromatics, *Environ. Sci. Technol.*, 2018, **52**, 6438–6447.

51 S. Marie-Rose, T. Belin, J. Mijoin, *et al.*, Catalytic combustion of polycyclic aromatic hydrocarbons (PAHs) over zeolite type catalysts: Effect of water and PAHs concentration, *Appl. Catal., B*, 2009, **90**, 489–496.

52 A. T. Aguayo, D. Mier, A. G. Gayubo, *et al.*, Kinetics of methanol transformation into hydrocarbons on a HZSM-5 zeolite catalyst at high temperature (400–550 °C), *Ind. Eng. Chem. Res.*, 2010, **49**, 12371–12378.